

# Design and characterisation of *ex situ* bulk MgB<sub>2</sub> superconductors containing a nanoscale dispersion of artificial pinning centres

G A B Matthews, J Liu , C R M Grovenor, P S Grant and S Speller 

Materials Department, University of Oxford, Parks Road, OX13PH, Oxford, United Kingdom

E-mail: [guillaume.matthews@materials.ox.ac.uk](mailto:guillaume.matthews@materials.ox.ac.uk)

Received 30 September 2019, revised 18 December 2019

Accepted for publication 8 January 2020

Published 27 January 2020



CrossMark

## Abstract

MgB<sub>2</sub> pellets containing a nanoscale dispersion of artificial pinning centres have been successfully manufactured through a powder metallurgy route based on the oxide dispersion strengthened (ODS) concept more usually used for steels and superalloys. Commercial MgB<sub>2</sub> powder and Y<sub>2</sub>O<sub>3</sub> nanopowder were mechanically alloyed in a high energy planetary ball mill and consolidated using the field assisted sintering technique. The composite powders were ball milled for different times up to 12 h and characterised by means of particle size analysis, x-ray diffraction (XRD) and scanning transmission electron microscopy (STEM). The microstructure and superconducting properties were characterised by density, XRD, STEM and magnetic property measurements. The powder microstructure comprised Y<sub>2</sub>O<sub>3</sub> particles dissolved into the MgB<sub>2</sub> matrix. After consolidation there was a near-uniform dispersion of precipitated YB<sub>4</sub> and MgO particles. A bulk 0.5 wt% Y<sub>2</sub>O<sub>3</sub>-MgB<sub>2</sub> composite showed the best superconducting performance with a significant improvement in  $J_c$  at high field compared with unmodified MgB<sub>2</sub>, and only a small reduction in  $T_c$ . The results suggest that the ODS concept is promising to improve the superconducting properties of MgB<sub>2</sub>.

Keywords: MgB<sub>2</sub>, bulk, microstructure, processing

(Some figures may appear in colour only in the online journal)

## 1. Introduction

Since the discovery of its superconducting properties in 2001 [1] MgB<sub>2</sub> has become a popular and promising material for superconductivity applications due to its interesting combination of properties. The critical temperature ( $T_c$ ) of 39 K is the highest of any binary compound at ambient pressure, and makes it more suitable for helium-free applications than other low temperature superconductors such as NbTi and Nb<sub>3</sub>Sn. In comparison to most high temperature superconducting compounds (HTS), MgB<sub>2</sub> does not contain any rare earth or toxic elements and is much easier to process [2]. Unlike HTS materials, MgB<sub>2</sub> bulks do not need to be processed in single grain (or low misorientation polycrystal) form because the larger coherence length in MgB<sub>2</sub> means that high angle grain boundaries do not act as weak links.

To improve the superconducting properties of MgB<sub>2</sub>, carbon doping or the addition of oxide particles to increase the critical current density ( $J_c$ ) has been used. Carbon doping has led to significant improvements in  $J_c$  at high field but also causes a severe reduction in  $T_c$  [3, 4]. Simple oxide additions in both *in situ* and *ex situ* processed materials can improve  $J_c$  values at high field, but decrease  $J_c$  at low field without having a significant effect on  $T_c$  [5–9]. Others have reported a decrease in  $J_c$  at both high and low fields [10, 11]. The effect of different additions on the superconducting properties of MgB<sub>2</sub> are summarised in table 1.

Most of these studies suggest that  $J_c$  improvements at high field is due to the presence of nanoscale pinning centres, although most reports do not show any direct evidence of pinning centres and their characteristics; the decrease in  $J_c$  at low field is also usually unexplained.

**Table 1.** Processing conditions and effect of different additions on the superconducting properties of MgB<sub>2</sub> bulk specimens. The effect on  $J_c$  at high and low field is represented by either an increase (↑) or decrease (↓) in  $J_c$  relative to unmodified MgB<sub>2</sub>, processed under the same conditions [5–11].

Author	Processing conditions	Additions	$H_{irr}$ 20 K (T)	$T_c$ (K)	$J_c(<2$ T) at 20 K	$J_c(>3$ T) at 20 K
[5]	<i>In situ</i> , 15 min at 900 °C	10 wt% Y <sub>2</sub> O <sub>3</sub>	5.5	38.3	—	↑
[7]	<i>In situ</i> , 30 min at 900 °C	10 wt% SiC + 10 wt% Y <sub>2</sub> O <sub>3</sub>	5	37	↓	↑
[10]	<i>Ex situ</i> , 3 min at 1150 °C	0.5 at% Bi <sub>2</sub> O <sub>3</sub>	3.6	38	↓	↓
[8]	<i>Ex situ</i> , 3 min at 1150 °C	1 at% TeO <sub>2</sub>	4.8	37.8	↓	↑
[9]	<i>Ex situ</i> , 3 min at 1150 °C	0.5 at% GeO <sub>2</sub>	5.1	38	↓	↑
[11]	<i>In situ</i> , 30 min at 800 °C	15 wt% TiO <sub>2</sub>	4.7	37.5	↓	↑
[6]	<i>In situ</i> , 5 min at 1000 °C	0.5 wt% Dy <sub>2</sub> O <sub>3</sub>	5	37.5	—	↑

This study investigates a new route to manufacture bulk MgB<sub>2</sub> pellets of up to 20 mm diameter, containing a nanoscale dispersion of artificial pinning centres based on the oxide dispersion strengthened (ODS) concept more usually used in steels and superalloys. The aim is to first dissolve Y<sub>2</sub>O<sub>3</sub> into the MgB<sub>2</sub> lattice by severe plastic work introduced by mechanical alloying, and second to re-precipitate Y-based nano particles during consolidation using the field assisted sintering technique (FAST), also known as resistive sintering [12] or spark plasma sintering [13]. The microstructure and superconducting properties of the bulks have been carefully characterised to provide a better understanding of the effect of the different microstructural features on  $J_c$  and  $T_c$  values.

## 2. Experimental details

Mixtures of pre-synthesised MgB<sub>2</sub> (purity: 99%, Alfa Aesar) and nano Y<sub>2</sub>O<sub>3</sub> (20–40 nm, purity: 99.999%, PI KEM Ltd) powders were sealed into stainless steel jars with stainless steel balls under an Ar atmosphere. The total mass of the powder was 10 g with a ball-to-powder ratio of 10:1. Mechanical alloying was conducted in a Fritsch P5 planetary ball mill rotated at 350 rpm in repeating cycles of 10 min of milling followed by a 20 min pause to prevent the powders from overheating. After different milling times (10 min, 1, 3, 6 and 12 h) the powders were recovered in a glove box under Ar.

For consolidation, the composite powders were poured into a 20 mm diameter graphite die lined with graphite paper and gently enclosed between two graphite punches. The powders were then cold compacted using a uni-axial pressure of 30 MPa before being transferred in the die into a Dr Fritsch DSP 507 FAST apparatus. The consolidation chamber was evacuated to 1 mbar and maintained at this pressure during the sintering process. The cold compacted green bodies were heated from room temperature to 1150 °C at a rate of 120 °C min<sup>-1</sup> then held for 5 min at 1150 °C before cooling down naturally. During the first heating step, the pressure was gradually increased to 50 MPa and then maintained during the high temperature dwell time at 1150 °C, before being progressively released during the final cooling step. The FAST

current and voltage passing through the die/punch/green body arrangement was 300–900 A and 0.6–1.2 V respectively.

The powders and FAST disks (20 mm in diameter and 4 mm in thickness) were characterised by several techniques, including x-ray diffraction (XRD), scanning transmission electron microscopy (STEM), powder particle analysis, density measurements and magnetometry. The XRD measurements were performed using a PANalytical Empyrean diffractometer with Cu<sub>K $\alpha$</sub>  radiation ( $\lambda = 0.154$  nm) at 40 kV and 40 mA. The lattice parameter, crystallite size, strain and weight fraction of the different phases present in the samples were estimated from the XRD spectra using Rietveld refinement (PANalytical HighScore Plus software). The weight fraction of the different phases was estimated by using the Hill and Howard method [14], implemented in HighScore Plus. Instrumental broadening of peaks was corrected using a Si standard analysed under the same scan conditions. The STEM analysis was performed in a JEOL 3000F at an accelerating voltage of 300 kV, equipped with a high angle annular dark field (HAADF) detector and an Oxford Instrument EDX detector. STEM specimens were prepared by cutting 3 mm disks from thin slices made from the consolidated pellets. The disks were then mechanically polished to approximately 100  $\mu$ m before being dimpled and finally thinned to perforation with a Fischione 1010 Ion Mill. The transmission Kikuchi diffraction (TKD) investigations were carried out in a Zeiss Merlin field emission gun (FEG) SEM system operating at 20 kV, equipped with a Bruker e-flash high-resolution electron back scattered diffraction (EBSD) detector and an OPTIMUS TKD head. Particle size analysis was performed using a Malvern Master-Sizer laser diffractometer by dispersing the powder in deionised water. The bulk density of the sintered samples was measured in isopropanol using the Archimede method. Magnetisation measurements were acquired with a quantum design physical property measurement system (PPMS) vibrating sample magnetometer (VSM) on cuboid samples cut from consolidated pellets, with dimensions of approximately 2 × 2 × 3 mm. The critical current density was calculated from the full magnetic hysteresis loops using Bean's model [15].

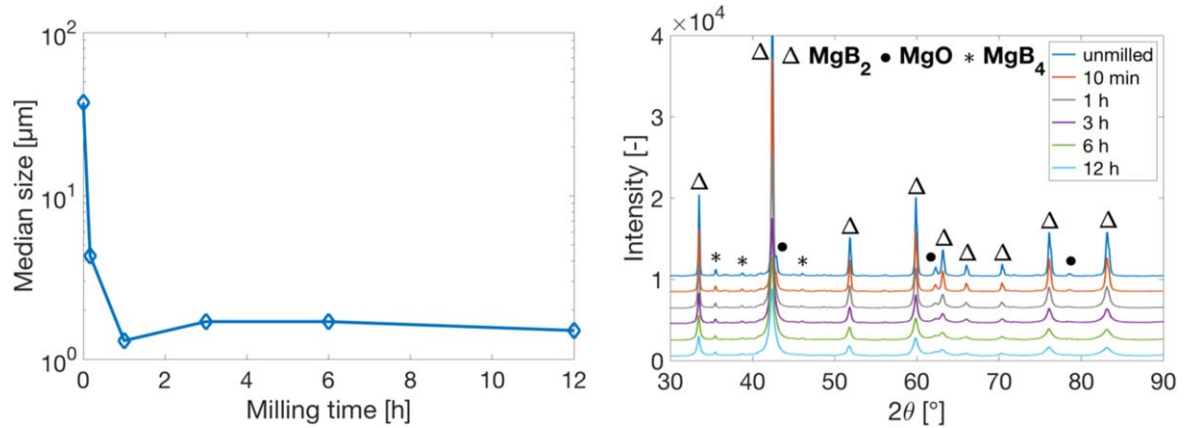


**Figure 1.** Median size (left) and XRD spectra (right) of the 0.5 wt%  $Y_2O_3$ - $MgB_2$  powders ball milled for different times.

**Table 2.** Characteristics of the 0.5 wt%  $Y_2O_3$ - $MgB_2$  powder ball milled for different times, estimated using Rietveld refinement.

Milling time	MgO (wt%)	MgB <sub>4</sub> (wt%)	MgB <sub>2</sub> crystallite size (nm)	MgB <sub>2</sub> strain (%)	MgB <sub>2</sub> <i>a</i> -axis (Å)	MgB <sub>2</sub> <i>c</i> -axis (Å)
0 h	4.7	7	99	0.11	3.0861	3.5242
10 min	5.1	6.9	110	0.13	3.0864	3.5237
1 h	6	7	95	0.23	3.0874	3.5249
3 h	8.1	7.8	81	0.31	3.0873	3.5251
6 h	9.5	9.1	71	0.45	3.0877	3.5266
12 h	10.9	11.1	46	0.52	3.0877	3.5276

### 3. Results and discussion

#### 3.1. $MgB_2$ based powders

The median particle diameter of the 0.5 wt%  $Y_2O_3$ - $MgB_2$  composite powder as a function of milling time and their corresponding XRD spectra are shown in figure 1. There was an initial sharp reduction in particle diameter from approximately 40  $\mu m$  for the pristine powder to 4  $\mu m$  after only 10 min of milling. The particle diameter then stabilised at 1.5  $\mu m$  after 1 h of milling, and this is usually interpreted as the point where the rate of fragmentation equals the rate of agglomeration.  $MgB_2$  is intrinsically relatively brittle, leading to the rapid diameter reduction.

The XRD spectra revealed three phases:  $MgB_2$ ,  $MgB_4$  and  $MgO$ . The small fraction of  $Y_2O_3$  added (0.5 wt%) was below the XRD detection limit, hence no  $Y_2O_3$  peaks were observed.  $MgB_4$  and  $MgO$  are impurities commonly found in  $MgB_2$  and often present in commercial powders [16, 17]. After milling, the characteristic peaks of all three phases in figure 1 decreased progressively in intensity and became broader, resulting in both an increase in inhomogeneous strain and/or a reduction in effective crystallite size, as shown in table 2. Table 2 summarises the results of Rietveld refinement of the XRD spectra. The pristine powder contained approximately 5 wt%  $MgO$  and 7 wt%  $MgB_4$ , and the fraction of these impurities increased with milling time. In particular, the  $MgO$  fraction increased up to 10.9 wt% after 12 h. Therefore, despite using an Ar filled glove box, it was not possible to fully exclude residual oxygen that reacted with the freshly formed surface of the  $MgB_2$  particles during ball milling. The

small increase in  $MgB_4$  fraction was probably a refinement artifact rather than a change in composition. The  $MgB_4$  peaks were relatively weak and difficult to fit during the Rietveld refinement, and the signal to noise ratio decreased with ball milling time which may have led to an overestimation of the total intensity of the  $MgB_4$  peaks relative to the total diffracted intensity.

As commonly seen in mechanically alloyed powders, the crystallite size of  $MgB_2$  decreased and the strain increased with milling time (table 2). Although the refinement of the particle diameter stopped after 1 h of milling, the XRD spectra suggested that refinement of the microstructure (crystallite size) continued. While qualitatively this behaviour is similar to that widely reported for ODS steels, it is perhaps surprising that a brittle compound shows essentially identical trends. Further, there was a gradual increase in the *a* and *c*-axis of the  $MgB_2$  lattice with increasing milling time. Yttrium has a larger atomic size (2.32 Å) than either magnesium or boron (1.73 and 1.92 Å respectively), and the increase in lattice volume may be due to the dissolution (and possible dissociation) of  $Y_2O_3$  into the  $MgB_2$  lattice. Again, similar phenomena are seen in metallic ODS solid solutions at long milling times [18, 19].

The composite powders were further characterized by STEM analysis. High angle annular dark field (HAADF) images of individual powder particles were acquired along with the corresponding Y and O EDX maps. Analysis was conducted on several particles for each milling condition and representative images and EDX maps of powder ball milled for 10 min, 1 and 12 h are shown in figure 2.

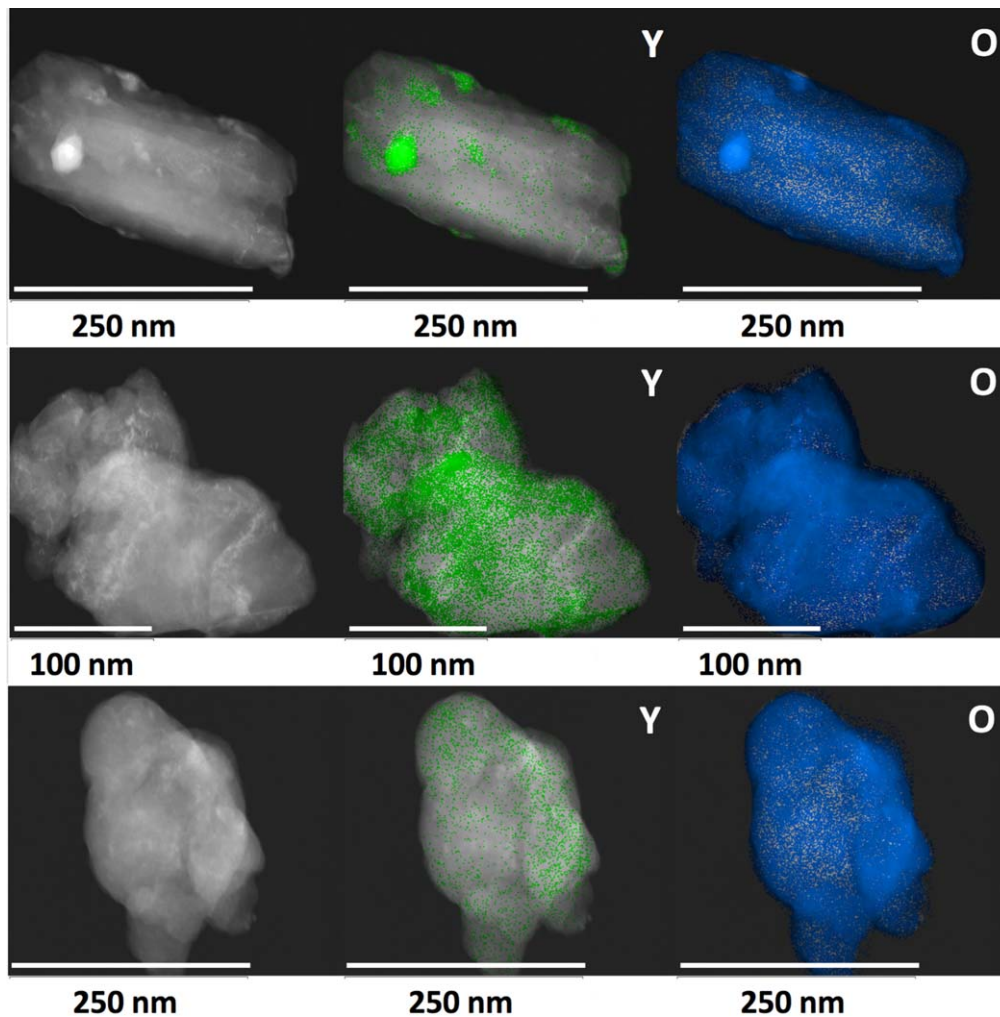


**Figure 2.** HAADF images, and corresponding Y and O EDX maps of 2 wt%  $Y_2O_3$ - $MgB_2$  powder ball milled for 10 min, 1 and 12 h (top to bottom).

After 10 min of milling, undissolved  $Y_2O_3$  particles of approximately 20–50 nm diameter were embedded in the  $MgB_2$  matrix. The corresponding Y and O maps indicated that Y and O concentrations were co-located. After 1 h of milling, the image contrast was more difficult to interpret due to the high concentration of defects (vacancies and dislocations) introduced by mechanical alloying, and few discrete  $Y_2O_3$  particles could be resolved. Again, in the EDX maps there were areas comparatively richer in both Y and O, but both elements were now more widely dispersed. This trend was confirmed after 12 h of milling where no  $Y_2O_3$  particles could be resolved and the EDX maps showed a much more homogeneous distribution of both Y and O. Consistent with the XRD results above, this suggests that the  $Y_2O_3$  nanoparticles have dissolved into the  $MgB_2$  lattice. In order to further investigate the evolution of the  $Y_2O_3$  phase during the mechanical alloying process, composite powders containing a much higher fraction of  $Y_2O_3$ , so that it might be more easily resolved, were fabricated. Figure 3 shows XRD spectra from  $MgB_2 + 10$  wt%  $Y_2O_3$  as a function of milling time.

The initial mix of powders showed a strong (222)  $Y_2O_3$  reflection, which was still visible after 10 min of milling.

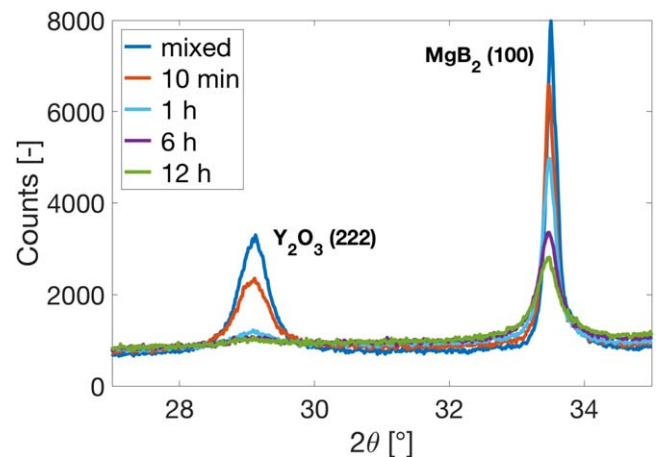


**Figure 3.** XRD spectra of 10 wt%  $Y_2O_3$ - $MgB_2$  composite powders showing the evolution of the (222)  $Y_2O_3$  and (100)  $MgB_2$  reflections with ball milling time.

However, this peak decreased in intensity after 1 h, and vanished at longer ball milling times. Thus it was concluded that for the composite powders, even when relatively large fractions of  $Y_2O_3$  were added, all the  $Y_2O_3$  was dissolved

**Table 3.** Composition and processing conditions for MgB<sub>2</sub> based pellets consolidated using the FAST.

Sample	Y <sub>2</sub> O <sub>3</sub> (wt%)	Milling time (h)	Temperature (°C)	Dwell time (min)	Pressure (MPa)	Heating rate (°C min <sup>-1</sup> )
MgB <sub>2</sub>	0	0	1150	5	50	120
0.5Ym1h	0.5	1	1150	5	50	120
0.5Ym12h	0.5	12	1150	5	50	120
2Ym12h	2	12	1150	5	50	120

**Table 4.** Density and estimated phase fractions by Rietveld analysis for bulk MgB<sub>2</sub>-based pellets consolidated by FAST.

Sample	MgO (wt%)	MgB <sub>4</sub> (wt%)	Relative density (%)	MgB <sub>2</sub> crystallite size (nm)	MgB <sub>2</sub> strain (%)	MgB <sub>2</sub> <i>a</i> -axis (Å)	MgB <sub>2</sub> <i>c</i> -axis (Å)
MgB <sub>2</sub>	8	13	93	151	0.14	3.0838	3.5279
0.5Ym1h	12.5	20.8	90	113	0.16	3.0836	3.5278
0.5Ym12h	15.2	17.3	87	87	0.2	3.0846	3.5287
2Ym12h	14.9	18.7	86	75	0.21	3.0844	3.5281

(presumably as dissociated Y and O) from the EDS maps) into the MgB<sub>2</sub> lattice during mechanical alloying. A further possibility, suggested for some cases of ODS steels, but for which there was no compelling evidence in this particular study, is that the Y<sub>2</sub>O<sub>3</sub> becomes first very finely divided and then effectively amorphous (glassy) due to the excessive cold work and ultra-high defect density induced by cold milling [20, 21].

### 3.2. Bulk MgB<sub>2</sub>

The FAST has been successfully used by several research groups to produce dense MgB<sub>2</sub> bulk samples [17, 22, 23]. Dancer *et al* [17] reported that MgB<sub>2</sub> with a relative density of 97% could be obtained by using a temperature of 1250°C and a pressure above 50 MPa. Aldica *et al* [23] achieved densities ranging from 95% to 97% using a temperature of 1150°C, a pressure of 95 MPa and dwell times between 1 and 20 min. The processing conditions used in this study were chosen based on these findings.

MgB<sub>2</sub>-based pellets were manufactured from different Y<sub>2</sub>O<sub>3</sub>-MgB<sub>2</sub> composite powders and processing conditions summarised in table 3. The three sample codes 0.5Ym1h, 0.5Ym12h and 2Ym12h correspond to bulk pellets manufactured from MgB<sub>2</sub> + 0.5 or 2 wt% Y<sub>2</sub>O<sub>3</sub> powders ball milled for 1 or 12 h.

The pellets were first characterized by density measurements and XRD. The bulk density, which includes both open and closed porosity, was measured using the Archimedes method, and the relative density calculated using the estimated phase fractions from the Rietveld refinement. As shown in table 4, longer milling times gave higher MgO fractions. Compared with the powders before consolidation, all consolidated pellets also showed a significant increase in MgB<sub>4</sub> fraction after sintering at 1150°C. The decomposition reaction 2MgB<sub>2</sub> → MgB<sub>4</sub> + Mg<sub>(g)</sub>, occurs above 900°C–1000°C [24, 25]. The unmodified MgB<sub>2</sub> pellet had the highest relative density of 93% while MgB<sub>2</sub> + Y<sub>2</sub>O<sub>3</sub> milled for 1 h had a slightly lower density of 90%, and MgB<sub>2</sub> +

Y<sub>2</sub>O<sub>3</sub> milled for 12 h had a density below 90%. This suggests that the addition of Y<sub>2</sub>O<sub>3</sub> and the increase in MgO fraction due to ball milling had a detrimental effect on densification, perhaps due to the higher intrinsic sintering temperature of MgO [26].

MgB<sub>2</sub> based pellets showed a small increase in MgB<sub>2</sub> crystallite size compared with their respective powders due to coarsening at 1150°C. Nonetheless, the relatively small crystallite size in the powder milled for 12 h was retained in the bulk samples, and finer than that of unmodified MgB<sub>2</sub>. The relatively high temperature consolidation—even for a short time of 5 min—significantly reduced the MgB<sub>2</sub> lattice strain, typically from 0.5% down to 0.2% after sintering.

The consolidated material was again studied by STEM, and typical HAADF images along with Y and O EDX maps of the 0.5Ym1h, 0.5Ym12h and 2Ym12h samples are shown in figure 4. For all the conditions we found relatively fine MgB<sub>2</sub> grains, typically of a diameter of a few hundred nanometres, and numerous MgO and YB<sub>4</sub> nano-particles. As shown in figures 4(c) and (d), fine 20–30 nm MgO particles were within MgB<sub>2</sub> grains, as well as coarser MgO up to 150 nm located at grain boundaries. Figures 4(c) and (d) show that the YB<sub>4</sub> precipitates have a diameter ranging from 20 to 60 nm, and were mainly located at the surface of the larger MgO particles and also within MgB<sub>2</sub> grains. No trace of discrete Y<sub>2</sub>O<sub>3</sub> particles was detected. The presence of YB<sub>4</sub> was confirmed by XRD and TKD, as shown in the example given in figure 5 for MgB<sub>2</sub> + 2 wt% Y<sub>2</sub>O<sub>3</sub>. Song *et al* [5] also found that YB<sub>4</sub> was formed in Y<sub>2</sub>O<sub>3</sub> doped MgB<sub>2</sub>. In fact, YB<sub>4</sub> can also be synthesised through the borothermal reduction of Y<sub>2</sub>O<sub>3</sub> at temperatures around 2000°C [27]. Although the sintering temperature (here of 1150°C) was lower, local temperatures in the FAST are known to sometimes be very much higher than the ‘bulk’ reading from a pyrometer or thermocouple, even if only for a few seconds. In addition, as previously suggested, Y may be dissolved in MgB<sub>2</sub> by milling and may react directly with MgB<sub>2</sub> on re-precipitation to form YB<sub>4</sub>. At the same time, dissolved oxygen precipitates as MgO.

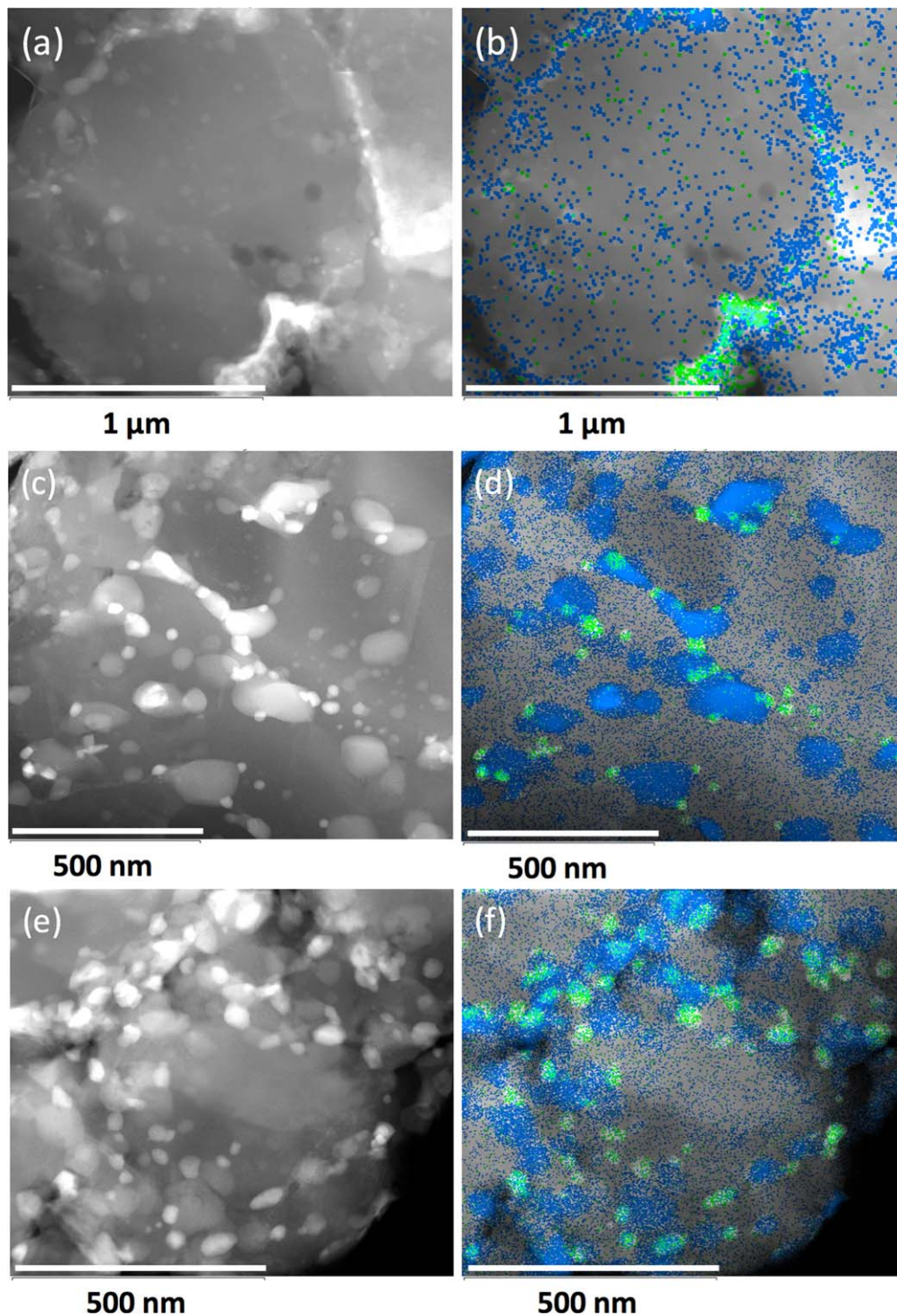


**Figure 4.** Typical HAADF images and Y (green) and O (blue) EDX maps of specimens (a), (b) 0.5Ym1h, (c), (d) 0.5Ym12h and (e), (f) 2Ym12h.

In a similar study, Mikheenko *et al* [6] also found that fine  $\text{DyB}_4$  particles precipitated during resistive sintering of  $\text{Dy}_2\text{O}_3$  doped  $\text{MgB}_2$ .

$\text{MgB}_2 + 0.5 \text{ wt}\% \text{ Y}_2\text{O}_3$  after 1 h of milling had a noticeably inhomogeneous  $\text{YB}_4$  particle distribution, which mainly formed large agglomerates at grain boundaries, as shown in figures 4(a) and (b). As expected, there was a higher  $\text{YB}_4$  fraction in  $\text{MgB}_2 + 2 \text{ wt}\% \text{ Y}_2\text{O}_3$  (shown in figures 4(e)

and (f)), with most precipitates located at grain boundaries. For  $\text{MgB}_2 + 0.5 \text{ wt}\% \text{ Y}_2\text{O}_3$  milled for 12 h the size distributions of the  $\text{MgO}$  and  $\text{YB}_4$  particles are shown in figure 6. The  $\text{YB}_4$  particles had a monomodal distribution with most diameters between 20 and 30 nm, and an average diameter of  $28 \pm 10 \text{ nm}$ . XRD spectra of  $\text{MgB}_2 + 10 \text{ wt}\% \text{ Y}_2\text{O}_3$  processed under the same conditions gave  $\text{YB}_4$  fractions high enough to be detected, and Rietveld analysis gave

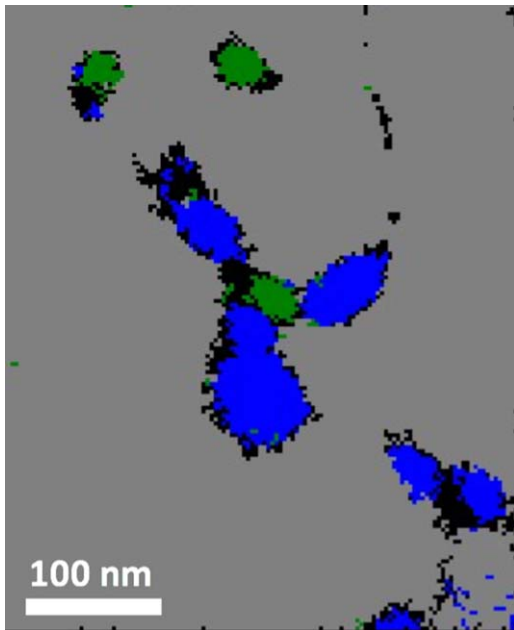


**Figure 5.** Typical TKD phase map from  $\text{MgB}_2 + 2 \text{ wt}\% \text{ Y}_2\text{O}_3$  showing  $\text{MgB}_2$  (grey),  $\text{YB}_4$  (green) and  $\text{MgO}$  (blue).

an average diameter of 35 nm, in good agreement with the STEM results.  $\text{MgO}$  showed a bimodal distribution composed of fine 20–50 nm and coarser 80–120 nm diameters, with an average diameter of  $60 \pm 30$  nm, again similar to the 50 nm extracted from the XRD measurements.

Overall, most of the  $\text{YB}_4$  particles nucleated on larger  $\text{MgO}$  particles, which suggested that  $\text{MgO}$  was present before  $\text{YB}_4$  precipitation, i.e. before sintering. These large  $\text{MgO}$  particles were probably pre-existing in the as-supplied  $\text{MgB}_2$  powder. The finer  $\text{MgO}$  particles were mainly located inside the  $\text{MgB}_2$  grains with a diameter similar to the  $\text{YB}_4$  precipitates, which may indicate they were formed and coarsened during the FAST process. This suggests that the addition and dissolution of  $\text{Y}_2\text{O}_3$  in the  $\text{MgB}_2$  matrix during mechanical alloying had the double effect of producing a fine dispersion of both  $\text{YB}_4$  and  $\text{MgO}$  during sintering. This is dissimilar to ODS alloys where predominantly  $\text{Y}_2\text{O}_3$  is re-precipitated, albeit with more complex transition phases sometimes involved, such as  $\text{Y-Ti-O}$  phases in  $\text{Fe-Cr-Ti}$  containing matrices [19].

The superconducting properties of the pellets are shown in figure 7 and summarised in table 5. Figure 7(a) shows the normalised susceptibility curves, with  $T_c$  values for unmodified  $\text{MgB}_2$ ,  $\text{MgB}_2 + 0.5 \text{ wt}\% \text{ Y}_2\text{O}_3$  milled for 1 h,  $\text{MgB}_2 + 0.5 \text{ wt}\% \text{ Y}_2\text{O}_3$  milled for 12 h and  $\text{MgB}_2 + 2 \text{ wt}\% \text{ Y}_2\text{O}_3$  milled for 12 h estimated as 38.7, 38.1, 37.7 and 37.2 K respectively.  $T_c$  in  $\text{MgB}_2$  is well-known to be affected by any deviation from an ideal  $\text{MgB}_2$  crystal structure, and is thus sensitive to doping, strain and defect concentrations, and this explains the degradation in  $T_c$  in our samples.  $\text{MgB}_2 + 0.5 \text{ wt}\% \text{ Y}_2\text{O}_3$  milled for only 1 h showed the smallest  $T_c$  reduction, whereas  $\text{MgB}_2 + 2 \text{ wt}\% \text{ Y}_2\text{O}_3$  milled for 12 h had the lowest  $T_c$  due to the higher strain.

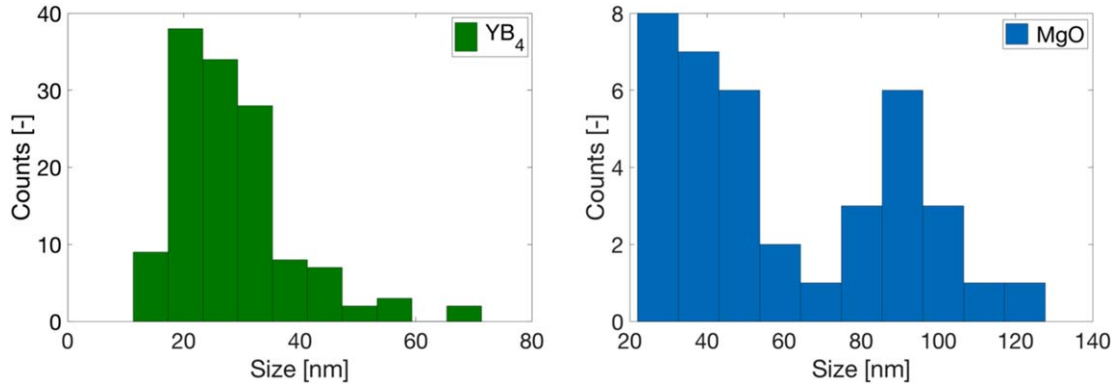
Nonetheless, all the pellets had only a small reduction in  $T_c$ , indicating that  $\text{Y}_2\text{O}_3$  does not have as severe an effect on  $T_c$  as carbon [4].

At 4.2 K, the high field properties are best represented on a log-scale  $J_c$ - $B$  plot, as shown in figure 7(b). Measurements at lower fields were often compromised by excessive flux jumps below 3 T, so this is not shown in the figure.  $\text{MgB}_2 + 0.5 \text{ wt}\% \text{ Y}_2\text{O}_3$  milled for 1 h showed no improvement compared with unmodified  $\text{MgB}_2$ , but by contrast  $\text{MgB}_2 + 0.5$  and  $2 \text{ wt}\% \text{ Y}_2\text{O}_3$  after 12 h milling both showed an appreciable improvement in  $J_c$  over the entire field range, with  $\text{MgB}_2 + 0.5 \text{ wt}\% \text{ Y}_2\text{O}_3$  (12 h) displaying the best performance. This strong difference in performance can be directly related to the STEM observations.  $\text{MgB}_2 + 0.5 \text{ wt}\% \text{ Y}_2\text{O}_3$  (1 h) showed a relatively poor distribution of  $\text{YB}_4$  particles, which formed agglomerates that were much larger than the coherence length of  $\text{MgB}_2$  ( $\xi = 5$ – $10$  nm [2]). In consequence, these agglomerates could not act as efficient pinning centres to improve  $J_c$ . On the contrary, STEM analysis showed that  $\text{MgB}_2 + 0.5$  or  $2 \text{ wt}\% \text{ Y}_2\text{O}_3$  (12 h) had a much more homogeneous dispersion of finer  $\text{YB}_4$  precipitates. Figures 4(e) and (f) also showed that for  $\text{MgB}_2 + 2 \text{ wt}\% \text{ Y}_2\text{O}_3$  (12 h) many particles were located at grain boundaries which could be detrimental to the grain connectivity and hinder macroscopic supercurrents. The improvement in  $J_c$  was probably a trade-off between an increase in pinning centre density and a degradation of grain connectivity. At 4.2 K,  $\text{MgB}_2 + 0.5 \text{ wt}\% \text{ Y}_2\text{O}_3$  (12 h) showed a three fold increase in  $J_c$  at 5 T and  $B_{irr}$  was improved by 1 T compared to unmodified  $\text{MgB}_2$ .

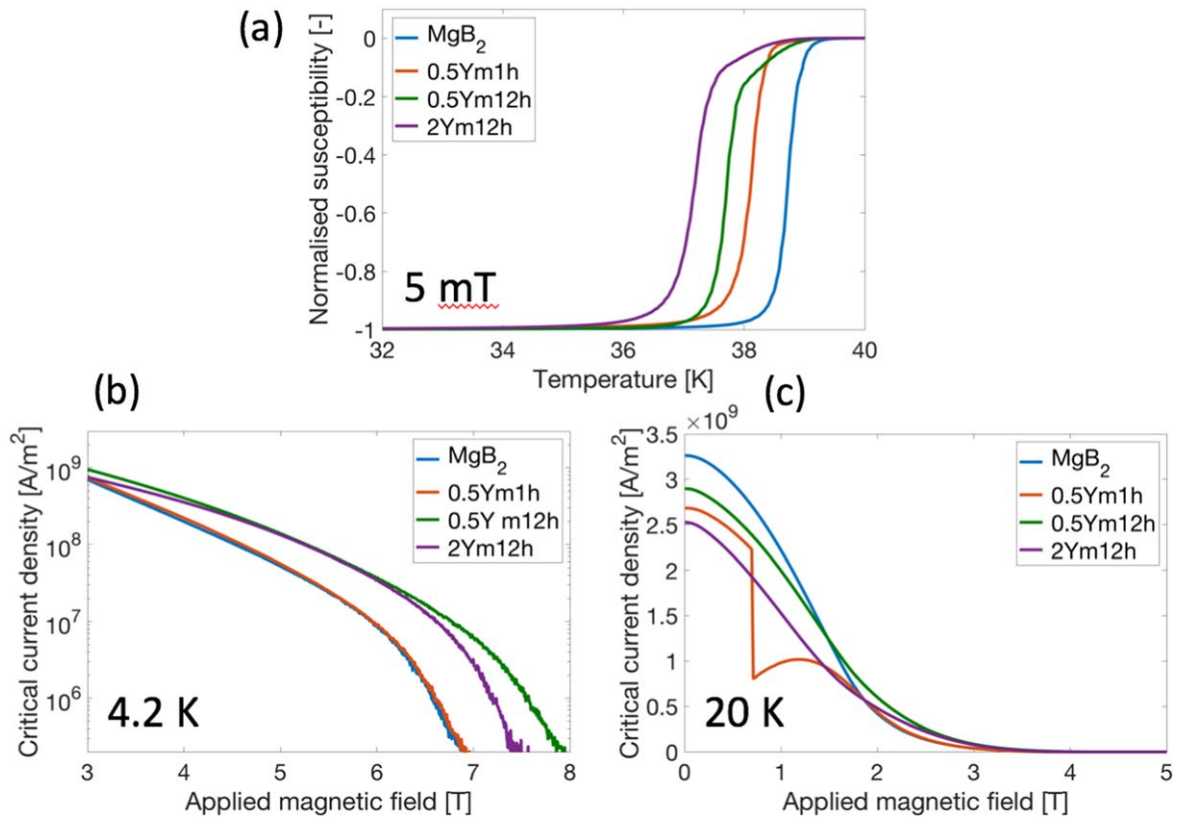
At 20 K, unmodified  $\text{MgB}_2$  showed the highest self-field  $J_c$  ( $J_{c0}$ ) followed by  $\text{MgB}_2 + 0.5 \text{ wt}\% \text{ Y}_2\text{O}_3$  (12 h),  $\text{MgB}_2 + 0.5 \text{ wt}\% \text{ Y}_2\text{O}_3$  (1 h), while  $\text{MgB}_2 + 2 \text{ wt}\% \text{ Y}_2\text{O}_3$  (12 h) had the lowest  $J_{c0}$ . Many parameters can influence  $J_{c0}$ , including the total superconducting fraction and grain connectivity. All the  $\text{MgB}_2 + \text{Y}_2\text{O}_3$  materials had a lower relative density and an impurity content significantly higher than unmodified  $\text{MgB}_2$ . The combination of these features controls the total superconducting fraction and explains why the unmodified  $\text{MgB}_2$  pellet, which had the highest total superconducting fraction, also showed the highest  $J_{c0}$ . Due to their similar density and composition, all the  $\text{Y}_2\text{O}_3$ -containing variants had a similar total superconducting fraction so that differences in  $J_{c0}$  may be due to differences in connectivity. For example, the STEM images in figures 4(a)–(f) suggested that  $\text{MgB}_2 + 0.5 \text{ wt}\% \text{ Y}_2\text{O}_3$  (12 h) had a better connectivity than both  $\text{MgB}_2 + 0.5 \text{ wt}\% \text{ Y}_2\text{O}_3$  (1 h) and  $\text{MgB}_2 + 2 \text{ wt}\% \text{ Y}_2\text{O}_3$  (12 h).

Figure 7(c) also shows that at 20 K,  $J_c$  at high field followed a similar trend to  $J_c(4.2 \text{ K})$ :  $\text{MgB}_2 + 0.5 \text{ wt}\% \text{ Y}_2\text{O}_3$  (12 h) had the best  $J_c$  of  $8.6 \times 10^7 \text{ A m}^{-2}$  with a two fold increase at 3 T and a 0.3 T improvement in  $B_{irr}$  compared with unmodified  $\text{MgB}_2$ .

These results are in good agreement with the studies of Song [5] and Mikheenko [6] who observed similar  $J_c$  improvements in  $\text{Y}_2\text{O}_3$  and  $\text{Dy}_2\text{O}_3$  doped  $\text{MgB}_2$ . The authors found that nano-scale  $\text{YB}_4$  or  $\text{DyB}_4$  particles were formed



**Figure 6.** Size distribution of  $\text{YB}_4$  and  $\text{MgO}$  particles found in the 0.5Ym12h specimen.



**Figure 7.** Normalised susceptibility curves of the bulk specimens (a) and  $J_c$ - $B$  curves at 4.2 K (b) and 20 K (c). The step observed in the 20 K 0.5Ym1h data is a flux jump.

**Table 5.** Superconducting properties of the pure  $\text{MgB}_2$  and composite bulk specimens.

Sample	$T_c$ (K)	$B_{irr}$ at 4.2 K (T)	$J_c$ at 4.2 K and 5 T ( $\text{A m}^{-2}$ )	$B_{irr}$ at 20 K (T)	$J_c$ at 20 K and 3 T ( $\text{A m}^{-2}$ )
$\text{MgB}_2$	38.7	6.6	$5.2 \times 10^7$	3.8	$4 \times 10^7$
0.5Ym1h	38.1	6.6	$5.6 \times 10^7$	3.8	$3.9 \times 10^7$
0.5Ym12h	37.7	7.6	$14 \times 10^7$	4.1	$8.6 \times 10^7$
2Ym12h	37.2	7.2	$13 \times 10^7$	4	$7.9 \times 10^7$

during sintering and acted as efficient pinning centres that enhanced  $J_c$ , in particular at high field. They reported higher  $J_c$  values than we have obtained in our specimens, but direct comparisons are difficult owing to the fact that both Song and Mikheenko used an *in situ* processing method which tends to lead to higher grain connectivity [28].

To analyse flux pinning mechanisms, the field dependence of the flux pinning force density,  $F_p = -J_c \times B$ , has been evaluated at 20 K. Figure 8(a) shows the normalised pinning force density,  $f_p = \frac{F_p}{F_{pmax}}$ , for each sample as a

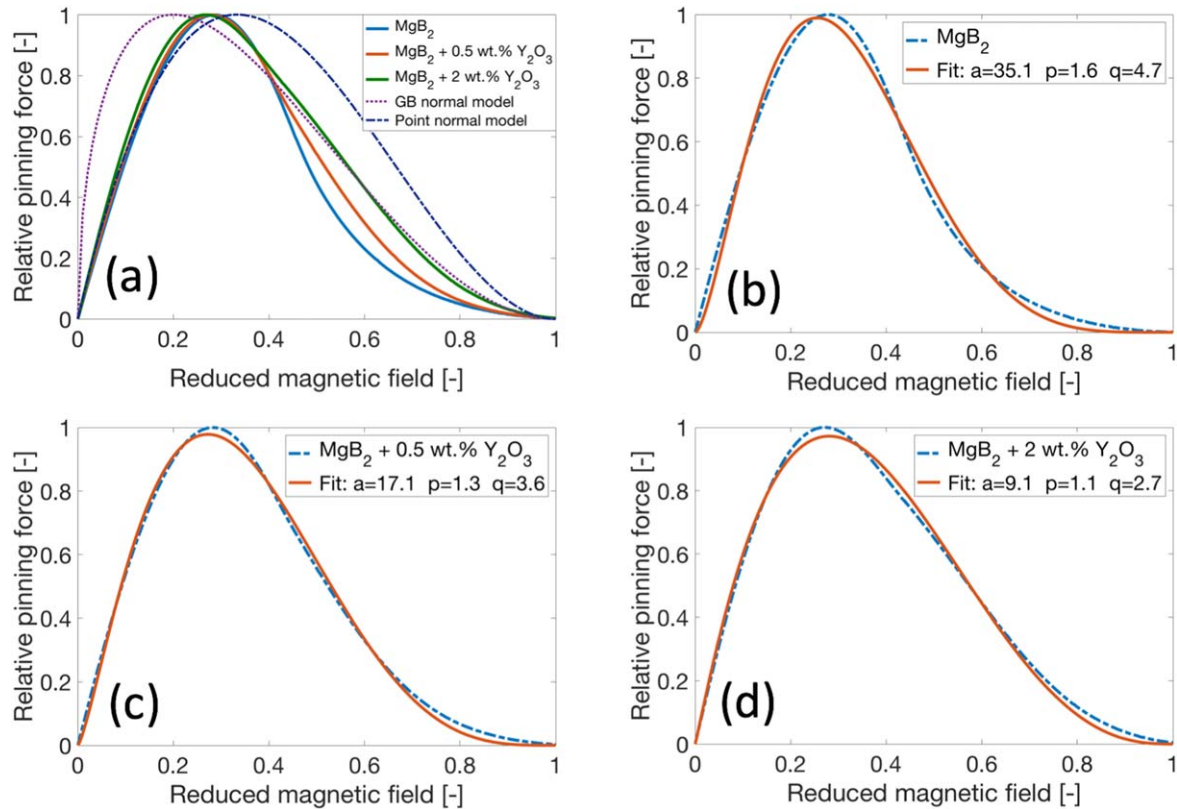


**Figure 8.** Normalised pinning force curves at 20 K of the bulk specimens (a) Specimens (b)–(d) and theoretical pinning models, (b) unmodified  $\text{MgB}_2$ , (c)  $\text{MgB}_2 + 0.5 \text{ wt}\% \text{ Y}_2\text{O}_3$  (12 h) and (d)  $\text{MgB}_2 + 2 \text{ wt}\% \text{ Y}_2\text{O}_3$  (12 h).

function of reduced field,  $b = \frac{B}{B^*}$ , where  $B^*$  is the field where  $J_c \rightarrow 0$ . The  $B^*$  values have been estimated using the method described by Martinez *et al*, which involves linear extrapolation of the low  $J_c$  sections of the Kramer curves,  $J_c^{\frac{1}{2}} B^{\frac{1}{2}}(B)$ , ignoring the zone close to  $B^*$  which is known to be strongly affected by flux creep [29]. Theoretical models of flux pinning based on the flux line shear mechanism predict that pinning curves take the functional form  $f_p \propto b^p(1-b)^q$ , with  $p$  and  $q$  values depending on the size and shape of the pins relative to the spacing of the flux line lattice and whether the pins are ‘normal’ material or weaker superconductor with a different Ginzburg Landau parameter ( $\Delta\kappa$  pinning) [30].

For polycrystalline  $\text{MgB}_2$  bulks, it is expected that the main pinning contributions will come from grain boundaries which give rise to ‘surface normal’ pinning ( $f_p \propto b^{\frac{1}{2}}(1-b)^2$ ,  $b_{peak} = 0.2$ ) and ‘point normal’ pinning ( $f_p \propto b(1-b)^2$ ,  $b_{peak} = 0.33$ ) presumably from small non-superconducting inclusions [31]. As can be seen in figure 8(a), the peak in the experimental flux pinning force curves for all three samples is at  $b_{peak} \approx 0.25$ , which is in between the peak positions expected for ideal ‘surface normal’ and ‘point normal’ pinning. This suggests that the pinning mechanisms in all three samples is similar and has contributions from both surface and point pins. However, the shapes of the experimental curves differ from each other and the theoretical curves. In particular, the high field portion of the flux pinning curves, above  $B_{peak}$  seems to get broader (and more similar to the theoretical curves) as the amount of  $\text{Y}_2\text{O}_3$  increases. Figures 8(b)–(d) shows the fits

of each experimental curve to a more general function  $f_p = ab^p(1-b)^q$ . The value of  $p$  is reasonably consistent (1.1–1.6), but  $q$  is found to increase with reducing doping concentration, with the undoped sample having  $q > 4$ , much higher than any of the standard models. This has been observed previously in polycrystalline  $\text{MgB}_2$  and other superconductors and has been attributed to a wide distribution of superconducting properties ( $B^*$ ) within the sample [29, 32]. This suggests that the undoped  $\text{MgB}_2$  has rather inhomogeneous superconducting properties, and this improves upon doping with  $\text{Y}_2\text{O}_3$ .

In addition, careful inspection of the 2 wt%  $\text{Y}_2\text{O}_3$  pinning curve shows evidence of a slight shoulder at around 0.5, which may indicate a slight contribution from another pinning mechanism such as ‘surface  $\Delta\kappa$ ’, which theoretically has a peak at  $b_{peak} = 0.6$ .

#### 4. Conclusion

Composite  $\text{Y}_2\text{O}_3$ – $\text{MgB}_2$  powders were successfully manufactured by mechanical alloying using high energy ball milling. XRD and STEM suggested that  $\text{Y}_2\text{O}_3$  slowly dissolved into the  $\text{MgB}_2$  matrix during mechanical alloying, by a process of  $\text{Y}_2\text{O}_3$  dissociation so that Y and O showed a relatively uniform distribution at the nanoscale after 12 h of milling. Milled powders showed significant residual strains up to 0.5% and crystallite sizes of 50–100 nm. Bulk pellets were manufactured using FAST and presented a complex microstructure

composed of a few hundred nanometres MgB<sub>2</sub> grains and a fine dispersion of nanoscale YB<sub>4</sub> and MgO precipitates. After only 1 h of milling, the YB<sub>4</sub> dispersion was relatively inhomogeneous with large agglomerates at grain boundaries, whereas after 12 h of milling YB<sub>4</sub> precipitates were 20 to 40 nm in diameter and more uniformly dispersed.

MgB<sub>2</sub> + 0.5 wt% Y<sub>2</sub>O<sub>3</sub> (12 h) showed a significant improvement in  $J_c(4.2\text{ K})$  at high field compared with unmodified MgB<sub>2</sub>, which was attributed to the relatively fine dispersion of nanoscale YB<sub>4</sub> and MgO precipitates acting as efficient pinning centres. In contrast, MgB<sub>2</sub> + 0.5 wt% Y<sub>2</sub>O<sub>3</sub> (1 h) showed no improvement due to a coarser and more inhomogeneous microstructure. MgB<sub>2</sub> + 2 wt% Y<sub>2</sub>O<sub>3</sub> (12 h) had poorer superconducting properties, probably due to a reduction in grain connectivity caused by the large fraction of insulating precipitates located at grain boundaries. Adding Y<sub>2</sub>O<sub>3</sub> slightly reduced  $T_c$  compared with unmodified MgB<sub>2</sub>, due to increased strain and defect concentrations that were not fully annealed out at 1150 °C.

The ODS concept was successfully applied to superconductors and has provided a significant improvement in  $J_c$  at high field because of the precipitation of a fine dispersion of YB<sub>4</sub> and MgO nano-particles that acted as efficient pinning centres for magnetic vortices. Future work will explore additional processing parameters such as the sintering temperature and time in order to maximise the performance of these ODS superconductors by refining further their nanoscale microstructure.

## Acknowledgments

The Authors would like to thank the UK Engineering and Physical Science Research Council and the Department of Materials, University of Oxford for financial support (EP/M508111/1, EP/P026427, Manufacture using Advanced Powder Processes and Process). The Authors acknowledge the use of characterisation facilities within the David Cockayne Centre for Electron Microscopy, Department of Materials, University of Oxford. The data are available at <https://doi.org/10.5287/bodleian:Y5Ne86zYJ>.

## ORCID iDs

J Liu  <https://orcid.org/0000-0002-9278-6463>

S Speller  <https://orcid.org/0000-0002-6497-5996>

## References

- [1] Nagamatsu J and Nakagawa N 2001 Superconductivity at 39 K in magnesium diboride *Nature* **410** 2–3
- [2] Buzea C and Yamashita T 2001 Review of superconducting properties of MgB<sub>2</sub> *Supercond. Sci. Technol.* **14** R115–46
- [3] Kim J H *et al* 2012 Microscopic role of carbon on MgB<sub>2</sub> wire for critical current density comparable to NbTi *NPG Asia Mater* **4** e3
- [4] Lee S, Masui T and Yamamoto A 2003 Carbon-substituted MgB<sub>2</sub> single crystals *Physica C* **397** 7–13
- [5] Song X and Larbalestier D C 2002 High critical current density and improved irreversibility field in bulk MgB<sub>2</sub> made by a scalable, nanoparticle addition route *Appl. Phys. Lett.* **81** 2026
- [6] Mikheenko P, Chen S K and MacManus-Driscoll J L 2007 Minute pinning and doping additions for strong, 20 K, in-field critical current improvement in MgB<sub>2</sub> *Appl. Phys. Lett.* **91** 1–4
- [7] Cai Q, Liu Y, Ma Z and Dong Z 2012 Superconducting properties of Y<sub>2</sub>O<sub>3</sub>/SiC Co-doped bulk MgB<sub>2</sub> *J. Supercond. Novel Magn.* **25** 357–61
- [8] Aldica G, Popa S, Enculescu M and Badica P 2012 Enhancement of critical current density and irreversibility field by Te or TeO<sub>2</sub> addition to MgB<sub>2</sub> bulk processed by spark plasma sintering *Scr. Mater.* **66** 570–3
- [9] Batalu D, Aldica G, Popa S, Kuncser A, Mihalache V and Badica P 2015 GeO<sub>2</sub>-added MgB<sub>2</sub> superconductor obtained by spark plasma sintering *Solid State Sci.* **48** 23–30
- [10] Burdusel M, Aldica G, Popa S, Enculescu M, Pasuk I and Badica P 2013 MgB<sub>2</sub> with addition of bi<sub>2</sub>O<sub>3</sub> obtained by spark plasma sintering technique *J. Supercond. Novel Magn.* **26** 1553–6
- [11] Xu G J 2004 Enhancement of the irreversibility field in bulk MgB<sub>2</sub> by TiO<sub>2</sub> nanoparticle addition *Physica C* **406** 95–9
- [12] Mikheenko P, Martinez E and MacManus-Driscoll J L 2007 Grain boundaries and pinning in bulk MgB<sub>2</sub> *Supercond. Sci. Technol.* **20** 264–70
- [13] Dancer C E J, Mikheenko P, Bevan A, Abell J S, Todd R I and Grovenor C R M 2009 A study of the sintering behaviour of magnesium diboride *J. Eur. Ceram. Soc.* **29** 1817–24
- [14] Hill J and Howard J 1987 Quantitative phase analysis from neutron powder diffraction data using the Rietveld method *J. Appl. Crystallogr.* **20** 467–74
- [15] Bean C P 1962 Magnetization of hard superconductors *Phys. Rev. Lett.* **8** 250–3
- [16] Kováč P and Grivel J-C 2004 The role of MgO content in *ex situ* MgB<sub>2</sub> wires *Supercond. Sci. Technol.* **17** 41–6
- [17] Dancer C E J, Prabhakaran D, Başoğlu M, Yanmaz E, Yan H, Reece M, Todd R I and Grovenor C R M 2009 Fabrication and properties of dense *ex situ* magnesium diboride bulk material synthesized using spark plasma sintering *Supercond. Sci. Technol.* **22** 095003
- [18] Zhang L, Ukai S, Hoshino T, Hayashi S and Qu X 2009 Y<sub>2</sub>O<sub>3</sub> evolution and dispersion refinement in Co-base ODS alloys *Acta Mater.* **57** 3671–82
- [19] Zhang H, Gorley M J, Chong K B, Fitzpatrick M E, Roberts S G and Grant P S 2014 An *in situ* powder neutron diffraction study of nano-precipitate formation during processing of oxide-dispersion-strengthened ferritic steels *J. Alloys Compd.* **582** 769–73
- [20] Dai L, Liu Y and Dong Z 2012 Size and structure evolution of yttria in ODS ferritic alloy powder during mechanical milling and subsequent annealing *Powder Technol.* **217** 281–7
- [21] Zhao Q, Yu L, Liu Y and Li H 2015 Morphology and structure evolution of Y<sub>2</sub>O<sub>3</sub> nanoparticles in ODS steel powders during mechanical alloying and annealing *Adv. Powder Technol.* **26** 1578–82
- [22] Lee S Y, Yoo S I, Kim Y W, Hwang N M and Kim D Y 2003 Preparation of dense MgB<sub>2</sub> bulk superconductors by spark plasma sintering *J. Am. Ceram. Soc.* **86** 1800–2
- [23] Aldica G, Popa S, Enculescu M, Pasuk I, Ionescu A M and Badica P 2018 Dwell time influence on spark plasma-sintered MgB<sub>2</sub> *J. Supercond. Novel Magn.* **31** 317–25
- [24] Liu Z-k, Schlom D G, Li Q and Xi X X 2001 Thermodynamics of the Mg-B system: implications for the deposition of films

- thermodynamics of the Mg-B system: implications for the deposition of MgB<sub>2</sub> thin films *Appl. Phys. Lett.* **78** 3678
- [25] Kario A, Nast R, Häler W, Rodig C, Mickel C, Goldacker W, Holzapfel B and Schultz L 2011 Critical current density enhancement in strongly reactive exsitu MgB<sub>2</sub> bulk and tapes prepared by high energy milling *Supercond. Sci. Technol.* **24** 075011
- [26] Gupta T 1971 Sintering of MgO: densification and grain growth *J. Mater. Sci.* **6** 25–32
- [27] Zaykoski J A, Opeka M M, Smith L H and Talmy I G 2011 Synthesis and characterization of YB<sub>4</sub> ceramics *J. Am. Ceram. Soc.* **94** 4059–65
- [28] Yamamoto A, Tanaka H, Shimoyama J i, Ogino H, Kishio K and Matsushita T 2011 Towards the realization of higher connectivity in MgB<sub>2</sub> conductors: *in situ* or sintered *ex situ*? *Japan. J. Appl. Phys.* **51** 010105
- [29] Martínez E, Mikheenko P, Millán A, Bevan A and Abell J S 2007 Flux pinning force in bulk MgB<sub>2</sub> with variable grain size *Phys. Rev. B* **75** 1–8
- [30] Dew-Hughes D 1974 Flux pinning mechanisms in type II superconductors *Phil. Mag.* **30** 293–305
- [31] Collings E W, Sumption M D, Bhatia M, Susner M A and Bohnenstiehl S D 2008 Prospects for improving the intrinsic and extrinsic properties of magnesium diboride superconducting strands *Supercond. Sci. Technol.* **21** 103001
- [32] Wordenweber R 1992 Mechanism of flux-line motion in high-temperature superconductors *Phys. Rev. B* **46** 3076–83